Analysis of nonlinear dynamics of a curved beam under gravity bias

Zhuhuan Wu,[1] Ke Huang,[1] Ning Wang,[1] Weicheng Huang,[2] Qingyun Wang,[1] and Jiaying Zhang[1,*]
[1]*School of Aeronautic Science and Engineering, Beihang University, Beijing 100191, China*
[2]*School of Engineering, Newcastle University, Newcastle upon Tyne NE1 7RU, United Kingdom*

Geometrical design endows the curved beam with asymmetric bistability without prestress, contributing to its widespread applications in integrated forming and microscale fabrication. However, the gravity bias inherent in these applications is rarely considered, undermining the accurate prediction of its real-world dynamics. To address this, a gravity-biased nonlinear dynamic model is established via Hamilton's principle and reduced to a Duffing-type equation with a constant term using Galerkin's method. Numerical simulations show that both the inter-well oscillations and the contained vacillating behavior manifest as V-shaped regions in the excitation amplitude-frequency parameter space. Bifurcation analysis reveals that the left and right boundaries of the vacillating region correspond to saddle-node and period-doubling bifurcations, respectively, both of which can be theoretically predicted. Furthermore, gravity bias is shown to deepen the lower potential well. For an upward-curved beam, it enlarges the excitation range for inter-well motion when initiated from the upper equilibrium, while narrowing the range when starting from the lower one. The influence of key geometric parameters is also systematically examined. Base excitation experiments were conducted to equivalently simulate distributed force excitation, and the results validate the theoretical predictions. This work elucidates the effects of practical environmental conditions and structural parameters on the nonlinear dynamics of curved beams, thereby providing a foundation for the design of mechanical metamaterials and related engineered systems.

I. INTRODUCTION

Bistable beams can undergo large elastic deformation by snapping between two stable equilibrium states without requiring additional energy to maintain either configuration [1-5]. This bistability is typically introduced either by pre-buckling a straight beam with an axial force [6] or by fabricating it with an initial curvature [5,7]. Compared to their buckled counterparts, curved beams can achieve bistability without prestress, which facilitates integrated forming and microscale fabrication [8-11]. As a result, they have found broad applications in mechanical metamaterials [12-15], mechanical logic gates [16,17], microelectromechanical systems (MEMS) [10,18,19], actuators [9,11], dampers [20,21], energy absorption [22,23], and energy harvesting [24,25] by utilizing the switching between two stable states.

Compared with quasi-static loading, recent work has found that dynamic excitation can greatly reduce the forcing amplitude required for state switching [26]. Hasan et al. [27] demonstrated that adding a static bias force to harmonic excitation effectively expands the amplitude-frequency range for steady-state switching, thereby enabling reliable transitions. However, these studies (including that of Hasan et al.) often ignore the most common and inevitable bias force: gravity. Such oversight may adversely affect predictions of system dynamics and stability [28]. Moreover, the large density-to-Young's-modulus ratio of commonly used compliant materials intensifies the gravitational effect on the structure [3,29]. Therefore, investigating the nonlinear dynamics of curved beams under the influence of gravity is crucial for simulating real-world conditions, accurately predicting their behavior, and guiding their design.

In this work, we investigate the nonlinear dynamics of a curved beam under gravity bias through theoretical analysis, numerical simulation, and experimental validation. Based on Hamilton's principle, a governing model of the gravity-biased curved beam is established and reduced via Galerkin's method to a Duffing-type equation with constant bias by retaining only the first mode. Analysis of the nonlinear restoring force and potential energy reveals that gravity shifts the force-displacement curve downwards and deepens the potential well associated with the lower stable state. We further examine several dynamic responses—including switching, reverting, vacillating, and intra-well oscillations—under varying geometric dimensions, forcing amplitudes, and frequencies. Numerical results show that inter-well behaviors including reverting, switching, and vacillating form a distinct V-shaped region near the primary resonance in the forcing amplitude–frequency space. For an upward-curved bistable beam, gravity bias expands the parameter range for inter-well oscillations when motion initiates from the upper equilibrium, whereas it narrows the range for switching and inter-well dynamics when starting from the lower equilibrium. Additionally, bifurcation and chaotic characteristics are analyzed, with theoretically derived saddle-node and period-doubling bifurcation curves aligning closely with the boundaries of vacillating motion. Finally, a simple experimental method was implemented by transforming harmonic base excitation into equivalent force excitation, successfully validating the simplified Duffing model across different geometric parameters.

The remainder of this paper is organized as follows. Sec. II introduces the theoretical model of the gravity-biased

*jiaying.zhang@buaa.edu.cn

curved beam, leading to a simplified governing equation. In Sec. III, we analyze both the static and dynamic behaviors, including theoretical predictions of the bifurcation boundaries. Experimental validation of the model across varying parameters is provided in Sec. IV. Finally, we conclude with a summary of our findings in Sec. V.

II. MODELING AND THEORETICAL ANALYSIS

A. Gravity-biased curved beam model

The dynamic model of the curved beam, with the effect of gravity bias taken into account, is developed for further study. We consider a clamped-clamped curved beam with an upward arch configuration, a span L, width b, and thickness c, as illustrated in Fig. 1. Based on Hamilton's principle, the governing equation for the arch's dynamic profile $\hat{w}(\hat{x},\hat{t})$ under a harmonic distributed excitation is formulated as [30]

$$\begin{aligned}&\rho A\left(\frac{\partial^2\hat{w}}{\partial\hat{t}^2}-\hat{g}\right)+\hat{C}_\mathrm{d}\frac{\partial\hat{w}}{\partial\hat{t}}+EI\left(\frac{\partial^4\hat{w}}{\partial\hat{x}^4}-\frac{\partial^4\hat{w}_0}{\partial\hat{x}^4}\right)\\&-\frac{EA}{2L}\left\{\int_0^L\left[\left(\frac{\partial\hat{w}}{\partial\hat{x}}\right)^2-\left(\frac{\partial\hat{w}_0}{\partial\hat{x}}\right)^2\right]\mathrm{d}\hat{x}\right\}\frac{\partial^2\hat{w}}{\partial\hat{x}^2}=\hat{f}\cos\left(\hat{\Omega}\hat{t}\right),\end{aligned}\tag{1}$$

where the as-fabricated shape

$$\hat{w}_0(\hat{x})=-\frac{h}{2}\left[1-\cos\left(\frac{2\pi\hat{x}}{L}\right)\right],\tag{2}$$

with h denoting the initial arch height. In the equation, A represents the cross-sectional area, $I = bc^3/12$ is the moment of inertia, ρ and E are the material density and Young's modulus, respectively, and $\hat{C}_\mathrm{d}$ denotes the viscous damping coefficient. Additionally, the gravitational acceleration $\hat{g}$ is included to account for gravity bias, while the harmonic distributed force is characterized by amplitude $\hat{f}$ and frequency $\hat{\Omega}$.

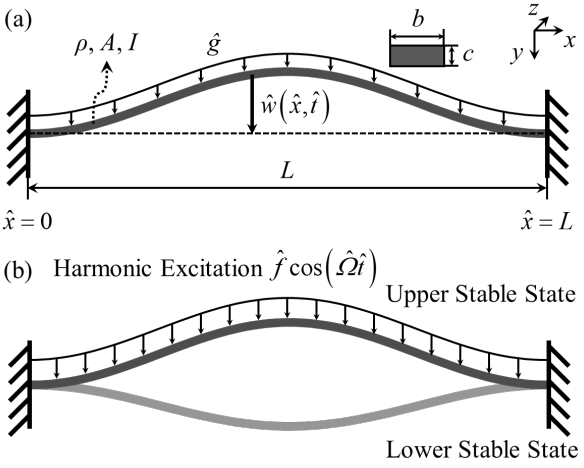

FIG. 1. Analytical model of the curved beam: (a) Schematic diagram of the upward-curved beam with defined parameters. (b) A harmonic distributed excitation is applied to enable switching between two stable states.

Next, the following parameters are introduced to further nondimensionalize Eq. (1):

$$\begin{aligned}&w=\frac{\hat{w}}{h},\ w_0=\frac{\hat{w}_0}{h},\ t=\frac{\hat{t}}{T},\ x=\frac{\hat{x}}{L},\ T=\sqrt{\frac{\rho AL^4}{EI}},\\&g=\frac{T^2}{h}\hat{g},\ Q=\frac{h}{c},\ C_\mathrm{d}=\frac{\hat{C}_\mathrm{d}L^2}{\sqrt{\rho AEI}},\ f=\frac{\hat{f}L^4}{EIh},\end{aligned}\tag{3}$$

and Eq. (1) is rewritten as

$$\begin{aligned}&\left(\frac{\partial^2w}{\partial t^2}-g\right)+C_\mathrm{d}\frac{\partial w}{\partial t}+\left(\frac{\partial^4w}{\partial x^4}-\frac{\partial^4w_0}{\partial x^4}\right)\\&-6Q^2\left\{\int_0^1\left[\left(\frac{\partial w}{\partial x}\right)^2-\left(\frac{\partial w_0}{\partial x}\right)^2\right]\mathrm{d}x\right\}\frac{\partial^2w}{\partial x^2}=f\cos\left(\hat{\Omega}Tt\right).\end{aligned}\tag{4}$$

To solve Eq. (4), we apply the method of separation of variables, by expressing the solution as a linear combination of products of spatial functions $\phi_i(x)$ and temporal variables $q_i(t)$:

$$w(x,t)=\sum_{i=1}^{n}q_i(t)\phi_i(x).\tag{5}$$

Galerkin's method is then employed to transform Eq. (4) into a set of coupled ordinary differential equations (ODEs). The shape functions are chosen as the vibration modes of the buckled beam, as they inherently satisfy the boundary conditions [19]:

$$\phi_i(x)=\begin{cases}\dfrac{1}{2}\left[1-\cos\left(N_ix\right)\right], & N_i=(i+1)\pi, \quad i=1,3,\ldots\\[2ex] \dfrac{1}{2}\left[1-2x-\cos\left(N_ix\right)\right. & \\ \quad\left.+\dfrac{2\sin\left(N_ix\right)}{N_i}\right], & N_i=2.86\pi,4.92\pi,\ldots \quad i=2,4,\ldots\end{cases}\tag{6}$$

Upon substituting the trial solution of Eq. (5) into Eq. (4), the weighted residual method is applied using the mode shape ϕ_j as the weight function. The resulting equation is integrated over the beam length, and by retaining only the first mode, the system is decoupled into:

$$\begin{aligned}&M_1\frac{\mathrm{d}^2q_1}{\mathrm{d}t^2}-F_1g+C_\mathrm{d}M_1\frac{\mathrm{d}q_1}{\mathrm{d}t}+\left(N_1q_1-G_1\right)\\&-6Q^2\left(D_1q_1^2-H_1\right)E_1q_1=F_1f\cos\left(\hat{\Omega}Tt\right),\end{aligned}\tag{7}$$

where

$$\begin{aligned}&M_1=\int_0^1\phi_1^2\mathrm{d}x=\frac{3}{8},\ F_1=\int_0^1\phi_1\mathrm{d}x=\frac{1}{2},\ N_1=\int_0^1\phi_1\frac{\mathrm{d}^4\phi_1}{\mathrm{d}x^4}\mathrm{d}x=2\pi^4,\\&G_1=\int_0^1\phi_1\frac{\mathrm{d}^4\phi_0}{\mathrm{d}x^4}\mathrm{d}x=-2\pi^4,\ D_1=\int_0^1\left(\frac{\mathrm{d}\phi_1}{\mathrm{d}x}\right)^2\mathrm{d}x=\frac{\pi^2}{2},\\&H_1=\int_0^1\left(\frac{\mathrm{d}\phi_0}{\mathrm{d}x}\right)^2\mathrm{d}x=\frac{\pi^2}{2},\ E_1=\int_0^1\phi_1\frac{\mathrm{d}^2\phi_1}{\mathrm{d}x^2}\mathrm{d}x=-\frac{\pi^2}{2},\end{aligned}\tag{8}$$

and

$$\phi_0(x)=w_0(x)=-\frac{1}{2}\left[1-\cos\left(2\pi x\right)\right].\tag{9}$$

Leveraging the relations $G_1 = -N_1$ and $H_1 = D_1$ in Eq. (8), we introduce a reference frequency ω_ref and the following

nondimensional parameters to further simplify the dynamic equation:

$$\omega_{\mathrm{ref}}=\sqrt{\left|\frac{N_1-K}{M_1}\right|},\quad \delta=\frac{C_{\mathrm{d}}}{\omega_{\mathrm{ref}}},\quad G=\frac{F_1 g}{M_1\omega_{\mathrm{ref}}^2},$$
$$l=\frac{N_1}{M_1\omega_{\mathrm{ref}}^2},\quad F=\frac{F_1 f}{M_1\omega_{\mathrm{ref}}^2},\quad \omega=\frac{\hat{\Omega}T}{\omega_{\mathrm{ref}}},\quad \tau=\omega_{\mathrm{ref}}t, \tag{10}$$

where

$$K=-6Q^2D_1E_1=\frac{3}{2}\pi^4Q^2. \tag{11}$$

Substituting Eqs. (10) and (11) into Eq. (7) reduces the governing equation to a standard biased Duffing equation with unit linear stiffness, which can be categorized into two types based on the value of geometric parameter Q:

$$\ddot{u}+\delta\dot{u}-u+pu^3+\left(p-1-G\right)=F\cos\left(\omega\tau\right),\quad p=l+1, \tag{12}$$

when $Q>2\sqrt{3}/3$;

$$\ddot{u}+\delta\dot{u}+u+su^3+\left(s+1-G\right)=F\cos\left(\omega\tau\right),\quad s=l-1, \tag{13}$$

when $Q<2\sqrt{3}/3$, where the overdot denotes differentiation with respect to the rescaled time τ, and q_1 is replaced by u to mitigate potential confusion in subscript notation later (see Supplemental Material, Sec. S1 [31] for detailed derivation). These formulations provide the basis for our subsequent numerical and theoretical investigation into the static and dynamic behaviors of the curved beam under gravity bias G. It should be noted that $Q=2\sqrt{3}/3$ corresponds to the critical point where the linear stiffness vanishes, which cannot be accommodated within the above normalization framework. Accordingly, the following analysis focuses on the case where $Q\neq 2\sqrt{3}/3$.

B. Theoretical prediction of nonlinear response

1. Saddle-node bifurcations

With the biased Duffing equations established, we now perform a theoretical analysis to predict the nonlinear response of the curved beam. Since we focus on the bistable dynamics of the system, Eq. (12) serves as the governing equation for theoretical study. By setting all time derivatives and excitation to zero, Eq. (12) becomes

$$-u+pu^3+q=0, \tag{14}$$

where $q=p-1-G$. The fixed points are then solved and denoted as $u_{\mathrm{f}i}$ (i = 1,2,3) in ascending order, where $u_{\mathrm{f}1}$ and $u_{\mathrm{f}3}$ are stable attractors and $u_{\mathrm{f}2}$ is an unstable saddle point. The frequency of small periodic orbits near each attractor is approximately given by

$$\omega_{\mathrm{f}i}=\sqrt{-1+3pu_{\mathrm{f}i}^2},\quad i=1,3. \tag{15}$$

Considering the primary resonance $\omega\approx\omega_{\mathrm{f}i}$ (i = 1,3) under weak damping and excitation, we rewrite Eq. (12) as

$$\ddot{u}+\varepsilon\tilde{\delta}\dot{u}-u+pu^3+q=\varepsilon^{\frac{3}{2}}\tilde{F}\cos\left(\omega\tau\right), \tag{16}$$

where $0<\varepsilon\ll 1$, $\tilde{\delta}$ and $\tilde{F}$ are $O(1)$ quantities. Assume that $\omega^2-\omega_{\mathrm{f}i}^2=O\left(\varepsilon\right)$ and set $\varepsilon\Omega=\omega^2-\omega_{\mathrm{f}i}^2$. Substituting $u=u_{\mathrm{f}i}+\sqrt{\varepsilon}v$ into Eq. (16) yields

$$\ddot{v}+\omega_{\mathrm{f}i}^2v=-\varepsilon^{\frac{1}{2}}\cdot 3pu_{\mathrm{f}i}v^2+\varepsilon\left[\tilde{F}\cos\left(\omega\tau\right)-pv^3-\tilde{\delta}\dot{v}\right]+O\left(\varepsilon^{\frac{3}{2}}\right). \tag{17}$$

Upon employing the invertible Van der Pol transformation

$$\begin{pmatrix}\eta\\ \mu\end{pmatrix}=\begin{bmatrix}\cos\frac{m}{n}\omega\tau & -\frac{n}{m\omega}\sin\frac{m}{n}\omega\tau\\ -\sin\frac{m}{n}\omega\tau & -\frac{n}{m\omega}\cos\frac{m}{n}\omega\tau\end{bmatrix}\begin{pmatrix}v\\ \dot{v}\end{pmatrix}, \tag{18}$$

with $m=n=1$, the second-order averaging method [32] is applied to reduce Eq. (17) to

$$\begin{cases}\dot{\eta}=\dfrac{\varepsilon}{2\omega_{\mathrm{f}i}}\left[-\tilde{\delta}\omega_{\mathrm{f}i}\eta+\Omega\mu-\beta_{\mathrm{f}i}\left(\eta^2+\mu^2\right)\mu\right],\\ \dot{\mu}=\dfrac{\varepsilon}{2\omega_{\mathrm{f}i}}\left[-\Omega\eta-\tilde{\delta}\omega_{\mathrm{f}i}\mu+\beta_{\mathrm{f}i}\left(\eta^2+\mu^2\right)\eta-\tilde{F}\right],\end{cases} \tag{19}$$

where $\beta_{\mathrm{f}i}=3/4\left(p-10p^2u_{\mathrm{f}i}^2/\omega_{\mathrm{f}i}^2\right)$ (i = 1,3). In polar coordinates satisfying $r=\sqrt{\eta^2+\mu^2}$ and $\theta=\arctan\left(\mu/\eta\right)$, Eq. (19) becomes

$$\begin{cases}\dot{r}=\dfrac{\varepsilon}{2\omega_{\mathrm{f}i}}\left(-\tilde{\delta}\omega_{\mathrm{f}i}r-\tilde{F}\sin\theta\right),\\ r\dot{\theta}=\dfrac{\varepsilon}{2\omega_{\mathrm{f}i}}\left(-\Omega r+\beta_{\mathrm{f}i}r^3-\tilde{F}\cos\theta\right).\end{cases} \tag{20}$$

The fixed point (r_{s}, θ_{s}) of Eq. (20) is obtained by setting both derivatives to zero, yielding

$$\begin{cases}\left(\tilde{\delta}\omega_{\mathrm{f}i}r_{\mathrm{s}}\right)^2+\left(\Omega r_{\mathrm{s}}-\beta_{\mathrm{f}i}r_{\mathrm{s}}^3\right)^2=\tilde{F}^2,\\ \theta_{\mathrm{s}}=\arctan\left(\dfrac{\tilde{\delta}\omega_{\mathrm{f}i}}{\Omega-\beta_{\mathrm{f}i}r_{\mathrm{s}}^2}\right).\end{cases} \tag{21}$$

Solving the third-order equation under the condition $\beta_{\mathrm{f}i}\neq 0$ reveals a supercritical saddle-node bifurcation of the fixed points at

$$\tilde{F}^2=\frac{2\Omega\left(\Omega^2+9\tilde{\delta}^2\omega_{\mathrm{f}i}^2\right)\mp 2\left(\Omega^2-3\tilde{\delta}^2\omega_{\mathrm{f}i}^2\right)^{\frac{3}{2}}}{27\beta_{\mathrm{f}i}}, \tag{22}$$

and a subcritical saddle-node bifurcation at

$$\tilde{F}^2=\frac{2\Omega\left(\Omega^2+9\tilde{\delta}^2\omega_{\mathrm{f}i}^2\right)\pm 2\left(\Omega^2-3\tilde{\delta}^2\omega_{\mathrm{f}i}^2\right)^{\frac{3}{2}}}{27\beta_{\mathrm{f}i}}, \tag{23}$$

where the upper (lower) sign corresponds to $\beta_{\mathrm{f}i}>0$ ($\beta_{\mathrm{f}i}<0$) in both equations.

Therefore, the harmonic response of Eq. (16) near the primary resonance takes the form:

$$u=u_{\mathrm{f}i}+\sqrt{\varepsilon}r_{\mathrm{s}}\cos\left(\omega\tau+\theta_{\mathrm{s}}\right)+O\left(\varepsilon\right). \tag{24}$$

Consequently, the stable and unstable solutions of Eq. (20) correspond to the stable and unstable periodic responses of the original system in Eq. (16), respectively (see Supplemental Material, Sec. S2 [31] for detailed derivation). The analysis indicates that a stable resonant response emerges near the bifurcation curve defined by Eq. (22), whereas a stable non-resonant response vanishes near the curve given by Eq. (23) [32].

2. Period-doubling bifurcation

Beyond the saddle-node bifurcations analyzed above, the nonlinear dynamics of the system are also profoundly influenced by the period-doubling bifurcation [33]. To capture this behavior, Eq. (12) is perturbed around the stable attractors u_{f1} and u_{f3} by introducing $u = \bar{u} + u_{\mathrm{fi}}$, which gives

$$\ddot{\bar{u}} + \delta\dot{\bar{u}} + \left(3pu_{\mathrm{fi}}^2 - 1\right)\bar{u} + 3pu_{\mathrm{fi}}\bar{u}^2 + p\bar{u}^3 = F\cos\left(\omega\tau\right). \quad (25)$$

Assuming the basic period-1 solution takes the form

$$\bar{u}^{(0)}\left(\tau\right) = a_1\cos\left(\omega\tau + \varphi\right). \quad (26)$$

To apply the asymptotic method, Eq. (25) is transformed to

$$\ddot{\bar{u}} + \omega^2\bar{u} + \varepsilon\bar{\alpha}\bar{u}^2 + \varepsilon^2\left[\bar{\delta}\dot{\bar{u}} + \bar{\beta}\bar{u}^3 + \sigma\bar{u} - \bar{F}\cos\left(\omega\tau\right)\right] = 0, \quad (27)$$

where

$$\begin{gathered}\varepsilon\bar{\alpha} = 3pu_{\mathrm{fi}}, \quad \varepsilon^2\bar{\beta} = p, \quad \varepsilon^2\bar{\delta} = \delta, \\ \varepsilon^2\sigma = 3pu_{\mathrm{fi}}^2 - 1 - \omega^2, \quad \varepsilon^2\bar{F} = F\end{gathered} \quad (28)$$

and $0 < \varepsilon \lll 1$.

We seek an approximate solution to Eq. (27) in the form of a power series of ε:

$$\begin{aligned}\tilde{u}\left(\varepsilon,\tau\right) = {} & a_1\cos\left(\omega\tau + \varphi\right) + \varepsilon u_1\left(a_1,\varphi,\tau\right) \\ & + \varepsilon^2 u_2\left(a_1,\varphi,\tau\right) + O\left(\varepsilon^3\right),\end{aligned} \quad (29)$$

where a_1 and φ are slowly varying variables governed by

$$\begin{cases}\dfrac{\mathrm{d}a_1}{\mathrm{d}\tau} = \varepsilon D_1\left(a_1,\varphi\right) + \varepsilon^2 D_2\left(a_1,\varphi\right) + O\left(\varepsilon^3\right), \\ \dfrac{\mathrm{d}\varphi}{\mathrm{d}\tau} = \varepsilon E_1\left(a_1,\varphi\right) + \varepsilon^2 E_2\left(a_1,\varphi\right) + O\left(\varepsilon^3\right).\end{cases} \quad (30)$$

Substituting Eqs. (29) and (30) into Eq. (27) and collecting terms of like powers of ε, we sequentially solve for the first and second-order corrections. Imposing the steady-state conditions

$$\frac{\mathrm{d}a_1}{\mathrm{d}\tau} = \frac{\mathrm{d}\varphi}{\mathrm{d}\tau} = 0, \quad (31)$$

along with the non-secularity conditions at each order, we obtain the intra-well periodic solution accurate to $O(\varepsilon^2)$:

$$\begin{aligned}&\tilde{u}\left(\tau\right) \\ &\approx a_1\cos\left(\omega\tau + \varphi\right) + a_0 + a_2\cos 2\left(\omega\tau + \varphi\right) + a_3\cos 3\left(\omega\tau + \varphi\right) \\ &= a_1\cos\left(\omega\tau + \varphi\right) - \frac{3pu_{\mathrm{fi}}}{2\omega^2}a_1^2 + \frac{pu_{\mathrm{fi}}}{2\omega^2}a_1^2\cos 2\left(\omega\tau + \varphi\right) \\ &\quad + \frac{1}{8\omega^2}\left(\frac{3p^2u_{\mathrm{fi}}^2}{2\omega^2} + \frac{p}{4}\right)a_1^3\cos 3\left(\omega\tau + \varphi\right).\end{aligned} \quad (32)$$

where the amplitude and phase of the fundamental harmonic are given by

$$\begin{cases}a_1 = \dfrac{F}{\sqrt{\left[\Omega_{\mathrm{non}}^2\left(a_1\right) - \omega^2\right]^2 + \delta^2\omega^2}}, \\ \varphi = \arctan\left[\dfrac{-\delta\omega}{\Omega_{\mathrm{non}}^2\left(a_1\right) - \omega^2}\right],\end{cases} \quad (33)$$

and

$$\Omega_{\mathrm{non}}^2\left(a_1\right) = \left(3pu_{\mathrm{fi}}^2 - 1\right) - \left(\frac{15p^2u_{\mathrm{fi}}^2}{2\omega^2} - \frac{3p}{4}\right)a_1^2.$$

To study the stability of solution (32), we introduce a small disturbance δu. Considering the time-translation invariance of the system, the variational equation of Hill's type is derived as

$$\delta\ddot{u} + \delta\cdot\delta\dot{u} + \delta u\left(\lambda_0 + \sum_{n=1}^{6}\lambda_n\cos n\omega\tau\right) = 0, \quad (34)$$

where

$$\begin{aligned}&\lambda_0 = 3p\left(a_0^2 + \frac{a_1^2}{2} + \frac{a_2^2}{2} + \frac{a_3^2}{2}\right) - 1, \quad \lambda_1 = 3p\left(2a_0a_1 + a_1a_2 + a_2a_3\right), \\ &\lambda_2 = 3p\left(\frac{a_1^2}{2} + 2a_0a_2 + a_1a_3\right), \quad \lambda_3 = 3p\left(a_1a_2 + 2a_0a_3\right), \\ &\lambda_4 = 3p\left(\frac{a_2^2}{2} + a_1a_3\right), \quad \lambda_5 = 3pa_2a_3, \quad \lambda_6 = \frac{3pa_3^2}{2}.\end{aligned} \quad (35)$$

Note that the period of time-dependent coefficient $\sum_{n=1}^{6}\lambda_n\cos n\omega\tau$ is $T_1 = T$, where $T = 2\pi/\omega$. The instability of solution (32) induced by period-doubling bifurcation is further investigated, by assuming the expression of $\delta u(\tau)$ according to Floquet theory as

$$\delta u\left(\tau\right) = \mathrm{e}^{\left(\sigma_1 - \frac{\delta}{2}\right)\tau}\sum_{n=1,3,5,\ldots}\left(b_{nc}\cos\frac{n\omega}{2}\tau + b_{ns}\sin\frac{n\omega}{2}\tau\right), \quad (36)$$

with a period of $2T_1$. Retaining only the terms for $n = 1$ and $n = 3$ in Eq. (36) and substituting them into Eq. (34), we apply the harmonic balance method and set the resulting fourth-order determinant to zero. This finally yields an eighth-order polynomial in σ_1:

$$\sigma_1^8 + d_6\sigma_1^6 + d_4\sigma_1^4 + d_2\sigma_1^2 + d_0 = 0, \quad (37)$$

where the detailed expressions of the coefficients can be found in the Supplemental Material, Sec. S3 [31]. From Eq. (36), when

$$\mathrm{Re}\left(\sigma_1 - \frac{\delta}{2}\right) \geq 0, \quad (38)$$

solution (32) is critically stable or unstable, due to the exponential growth of the double-period perturbation. The boundary of the period-doubling bifurcation in the parameter space of (ω,F) is thus predicted by solving Eq. (37), calculating the maximum real part of σ_1, and determining the region where it satisfies the instability criterion of Eq. (38) (see Supplemental Material, Sec. S3 [31] for detailed derivation).

III. NUMERICAL AND ANALYTICAL RESULTS

A. Nonlinear restoring force

We begin by analyzing the statics of the curved beam based on the approximate models given in Eqs. (12) and (13). When $Q > 2\sqrt{3}/3$, the nondimensional restoring force with gravity bias is expressed as

$$F_{\mathrm{static}}\left(u\right) = -u + pu^3 + \left(p - 1 - G\right), \quad (39)$$

thereby indicating a potential energy function described by

$$E_{\text{static}}(u) = -\frac{1}{2}u^2 + \frac{1}{4}pu^4 + (p-1-G)u - \left(\frac{1}{2}u_{\text{f}}^2 - \frac{3}{4}pu_{\text{f}}^4\right), \tag{40}$$

with the reference point of potential energy defined at $u = u_{\text{f3}}$ when $F_{\text{static}} = 0$ has three roots, or at $u = u_{\text{f}}$ when the equation admits only one root u_{f}. To investigate the force-displacement and energy landscapes under varying Q, a parametric study is conducted by altering the beam as-fabricated shallow arch height h, while keeping the thickness c constant. The basic parameter values are summarized in Table I.

TABLE I. Values of basic parameters.

Parameters	Meanings	Values
L	Beam span	0.06 m
b	Beam width	0.01 m
c	Beam thickness	1×10^{-3} m
ρ	Beam density	1082 kg/m^3
E	Young's modulus	0.74 MPa
$\hat{g}$	Gravity acceleration	9.8 m/s^2
$\hat{C}_{\text{d}}$	Viscous damping coefficient	0.2 Pa·s

The numerically computed nonlinear restoring force and potential energy are plotted against displacement in Figs. 2(a) and 2(b), respectively. As shown in the figures, the restoring force exhibits a negative stiffness region. When $Q >$ 2.52, the peak value of the force-displacement diagram exceeds zero, resulting in three distinct intersection points with $F_{\text{static}} = 0$. With $u = 0$ set at the flat beam configuration rather than at an equilibrium, these three intersections correspond to the appearance of three equilibria, indicating bistability. For $2\sqrt{3}/3 < Q < 2.52$, however, the arch is shallow and the gravity dominates over the initial geometric asymmetry. Consequently, the force-displacement curve intersects the line at only one point near $u = 1$, implying the disappearance of the upper stable state, and the system is stable only at the lower equilibrium.

When $Q < 2\sqrt{3}/3$, the nondimensional restoring force is in the form

$$F_{\text{static}}(u) = u + su^3 + (s+1-G), \tag{41}$$

and the potential energy yields

$$E_{\text{static}}(u) = \frac{1}{2}u^2 + \frac{1}{4}su^4 + (s+1-G)u + \left(\frac{1}{2}u_{\text{f}}^2 + \frac{3}{4}su_{\text{f}}^4\right), \tag{42}$$

where the reference point of potential energy is defined at $u = u_{\text{f}}$, the unique attractor of the system. With the restoring force maintaining positive stiffness throughout the displacement range, the beam remains monostable. The potential energy thus exhibits a single well only at the lower equilibrium, as the shallow arch is insufficient to sustain an upper stable state under gravity. This behavior is shown in Figs. 2(c) and 2(d).

Furthermore, to evaluate the effect of gravity, the force-displacement and potential energy profiles are compared in the presence and absence of the gravity bias term G at a fixed value of $Q = 5.22$, as shown in Figs. 2(e) and 2(f). The results demonstrate that the gravity bias induces a downward shift in the force-displacement curve, and shallows the potential well at the upper stable state $u = u_{\text{f1}}$ relative to the lower stable state. Consequently, the positions of the equilibrium points are altered: both stable equilibria shift downward, while the saddle point between them shifts upward due to its presence in the region of negative stiffness. Thus, when a constant gravitational force is applied, the displacements of the stable and unstable equilibria move in opposite directions.

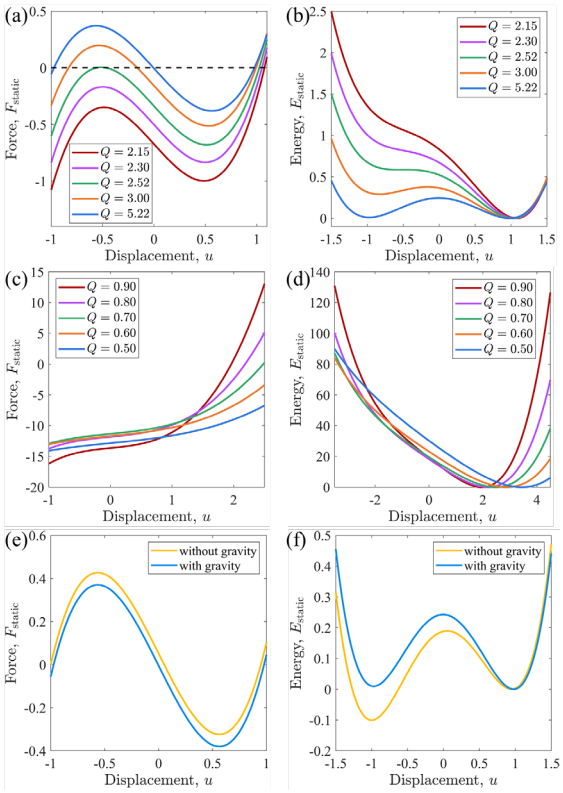

FIG. 2. Force-displacement and potential energy profiles under varying Q. (a), (c) Nondimensional restoring force versus displacement for $Q > 2\sqrt{3}/3$ and $Q < 2\sqrt{3}/3$, respectively. (b), (d) Potential energy versus displacement with the reference point set at $u = u_{\text{f3}}$ for $Q > 2\sqrt{3}/3$ and the unique stable equilibrium $u = u_{\text{f}}$ for $Q < 2\sqrt{3}/3$, respectively. (e), (f) Comparisons of the force-displacement relation and the potential energy with and without gravity bias for $Q = 5.22$.

B. Steady-state behavior patterns

We next examine the dynamics of the curved beam under the combined influence of harmonic excitation and gravity, with the initial height fixed at $h = 5.22$ mm (i.e., $Q = 5.22$). Because prior studies indicate that bistable structures can switch between stable configurations with relatively low energy input near their primary resonance [26,34-36], our analysis focuses on the nonlinear responses in this regime. Nonlinear phenomena associated with superharmonic or subharmonic resonances fall outside the scope of the present study.

Numerical solutions of the double-well Duffing equation reveal that the steady-state behaviors of this bistable system can be classified into four distinct categories [26,27]: (i) Switching: The oscillation initiates in one potential well and ultimately stabilizes in the other, as shown in Figs. 3(a) and

3(b). (ii) Reverting: The oscillation starts in one well, transiently crosses to the other, but eventually returns to and settles in the original well, as shown in Figs. 3(c) and 3(d). (iii) Vacillating: The oscillation persists in crossing between the two wells without settling in either, as shown in Figs. 3(e) and 3(f). (iv) Intra-well: The oscillation is confined to and remains within a single potential well, as shown in Figs. 3(g) and 3(h). The first three types are collectively referred to as inter-well oscillations.

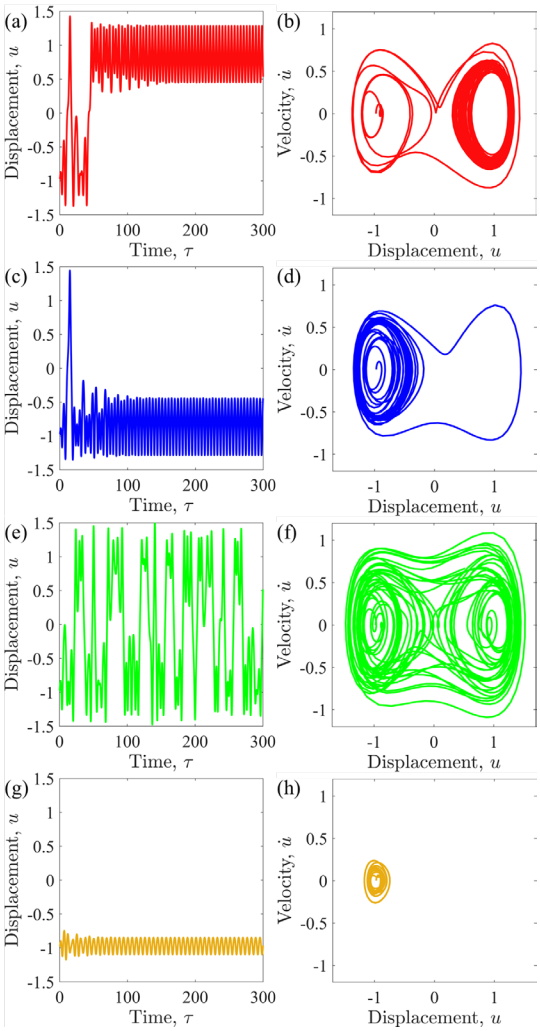

FIG. 3. Categories of steady-state behaviors at $Q = 5.22$. Time-domain responses and corresponding phase portraits are shown for different parameters, all starting from $(u,\dot{u}) = (u_{f1},0)$. (a), (b) Switching dynamics under periodic excitation at (ω,F) = (1.400,0.230). (c), (d) Reverting dynamics for (ω,F) = (1.350,0.190). (e), (f) Vacillating dynamics for (ω,F) = (1.180,0.260). (g), (h) Intra-well periodic oscillation for (ω,F) = (1.000,0.120).

To systematically characterize the nonlinear dynamics, the steady-state behavior patterns are mapped in the (F,ω) parameter space, with simulations initialized from either the upper stable state $u = u_{f1}$ or the lower stable state $u = u_{f3}$. Equation (12) is solved numerically using the fourth-order Runge-Kutta method. The nondimensional forcing frequency and amplitude are varied within $0.80 \le \omega \le 1.80$ and $0.03 \le F \le 0.30$, respectively, with uniform increments of $\Delta\omega = 0.002$ and $\Delta F = 0.001$. Each simulation is conducted over a total duration of $\tau_{tot} = 400T$, where $T = 2\pi/\omega$ is the excitation period. During computation, we record whether the trajectory visited the other potential well in the transient stage.

From the simulated responses, the last 50 excitation periods are analyzed to determine the steady-state behavior. The maximum and minimum displacements in this interval, denoted as $u_s^{max} = \max\{u(\tau)|\tau \in \{\text{last 50 cycles}\}\}$ and $u_s^{min} = \min\{u(\tau)|\tau \in \{\text{last 50 cycles}\}\}$, are computed [26]. The classification is based on these extreme values relative to the saddle point u_{f2}, combined with the transient record:

(i) Switching behavior: Identified when both u_s^{max} and u_s^{min} lie beyond u_{f2} in the non-initial well—that is, when $(u_s^{max} - u_{f2})$ and $(u_s^{min} - u_{f2})$ share the same sign and correspond to the opposite potential well from the initial condition.

(ii) Reverting behavior: Classified when both extremes remain in the initial well relative to u_{f2}, but the transient record confirms a visit to the other well, after which the system ultimately returns to the initial well.

(iii) Vacillating behavior: Determined when $u_s^{max} > u_{f2} > u_s^{min}$, indicating persistent cross-well oscillation in the steady state.

(iv) Intra-well behavior: Defined when both extremes lie in the initial well relative to u_{f2} and no transient crossing to the other well is recorded, confirming oscillation confined to the initial potential well.

Using the baseline parameters from Table I, the value of Q is varied by adjusting the as-fabricated arch height h. The resulting steady-state behavior patterns, obtained using the above numerical and classification framework, are presented in Fig. 4, providing a comprehensive view of the system's nonlinear response topology.

As shown in Fig. 4, the primary inter-well resonance of the curved beam under coupled gravity bias and harmonic excitation manifests as a V-shaped region in the (F,ω) parameter space, which is typical for forced escape systems [37,38]. Due to geometric asymmetry and gravitational effects, the behavior patterns differ depending on whether the oscillation initiates from the upper stable state $u = u_{f1}$ or the lower stable state $u = u_{f3}$, as compared between Figs. 4(a) and 4(d), Figs. 4(b) and 4(e), and Figs. 4(c) and 4(f) at the same Q value. With decreasing Q, the potential well disparity increases (see Fig. 2(b)), leading to more pronounced differences in the steady-state behavior patterns between the two initial conditions.

When oscillations start from the upper stable state $u = u_{f1}$, a decrease in Q substantially widens the parameter region for switching behavior, which becomes dominant among inter-well oscillations, as shown in Figs. 4(a)–(c). Concurrently, the parameter ranges for reverting and vacillating behaviors narrow, while the overall region for inter-well motion expands. In contrast, for motion initiating from the lower stable state $u = u_{f3}$, the parameter ranges for both switching and vacillating behaviors shrink as Q decreases, as illustrated in Figs. 4(d)–(f). A lower Q also reduces the total parameter region for inter-well oscillation, indicating that the system becomes less likely to escape from the potential well.

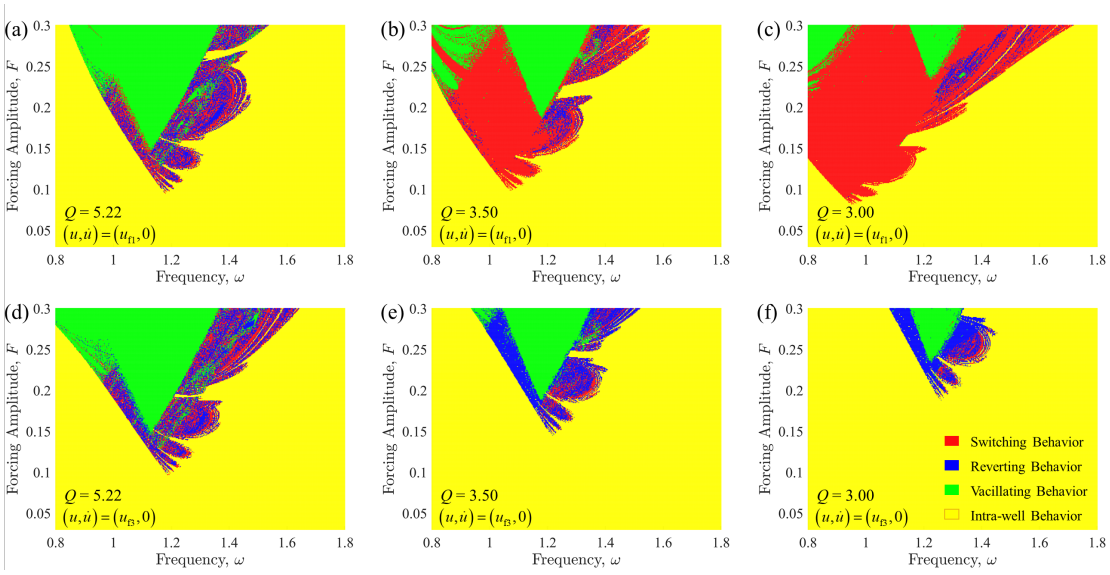

FIG. 4. Steady-state behavior patterns in the (F,ω) parameter space under different values of Q and initial conditions. (a) Q = 5.22, with the initial state at $(u,\dot{u})=(u_{\mathrm{f1}},0)$. (b) Q = 3.50, initial state at $(u,\dot{u})=(u_{\mathrm{f1}},0)$. (c) Q = 3.00, initial state at $(u,\dot{u})=(u_{\mathrm{f1}},0)$. (d) $Q=5.22$, initial state at $(u,\dot{u})=(u_{\mathrm{f3}},0)$. (e) $Q=3.50$, initial state at $(u,\dot{u})=(u_{\mathrm{f3}},0)$. (f) $Q=3.00$, initial state at $(u,\dot{u})=(u_{\mathrm{f3}},0)$.

To further investigate the influence of gravity bias on the dynamics of the curved beam, we compare the steady-state behavior patterns of the system with and without gravitational effects, starting from either the upper or lower stable state. It is important to note that when gravity is neglected, the positions of the fixed points change accordingly. These new fixed points, determined from

$$-u+pu^3+(p-1)=0, \tag{43}$$

are denoted as u'_{fi} (i = 1,2,3) in ascending order, with u'_{f1} and u'_{f3} being stable attractors and u'_{f2} an unstable saddle point.

For a specific value of Q = 5.22, the steady-state behavior patterns initialized from the upper equilibrium are presented in Figs. 5(a) (with gravity) and 5(b) (without gravity), with a direct comparison shown in Fig. 5(c). Similarly, results starting from the lower equilibrium are provided in Figs. 5(d) (with gravity) and 5(e) (without gravity), alongside their comparison in Fig. 5(f).

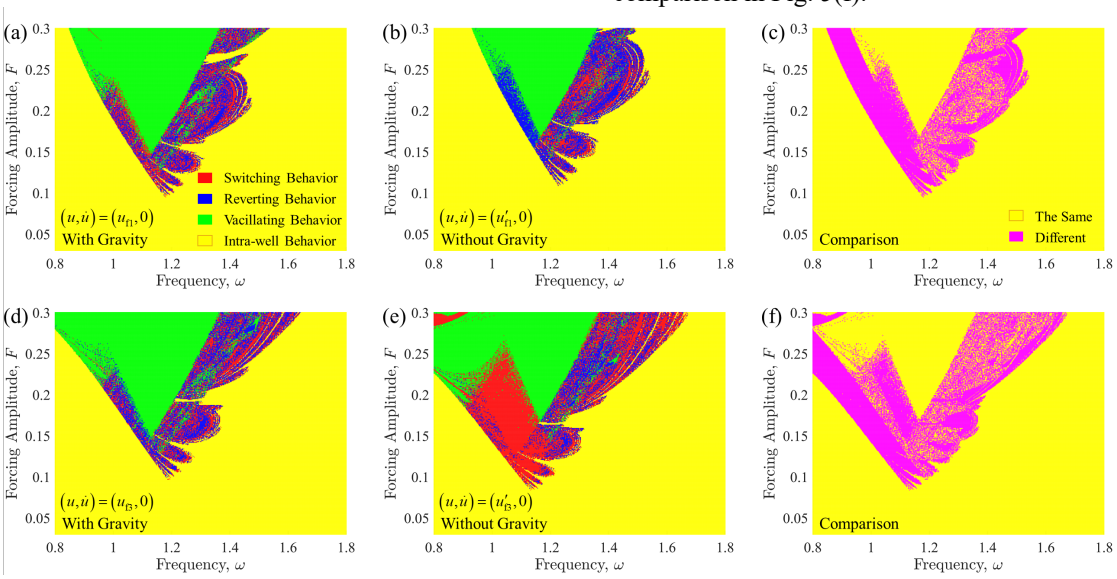

FIG. 5. Comparison of steady-state behavior patterns in the (F,ω) parameter space at $Q=5.22$, highlighting the effect of gravity bias. Results are shown for simulations initialized from the upper equilibrium position, $(u,\dot{u})=(u_{\mathrm{f1}},0)$ with gravity and $(u,\dot{u})=(u'_{\mathrm{f1}},0)$ without. (a) With gravity. (b) Without gravity. (c) Comparison of (a) and (b). Corresponding results for the lower equilibrium position, $(u,\dot{u})=(u_{\mathrm{f3}},0)$ with gravity and $(u,\dot{u})=(u'_{\mathrm{f3}},0)$ without: (d) With gravity. (e) Without gravity. (f) Comparison of (d) and (e).

As shown in Figs. 5(a)–(c), when the motion initiates from the upper stable state, the presence of gravity bias expands the parameter region for inter-well oscillation, indicating a higher propensity for the system to escape from the upper potential well. This effect particularly facilitates switching behavior in the low-frequency regime, which is otherwise dominated by the reverting behavior when gravity is neglected. In contrast, for oscillations starting from the lower stable state (Figs. 5(d)–(f)), gravity significantly narrows the parameter range associated with switching behavior, with the vacillating and reverting types becoming predominant. Moreover, the overall region of inter-well oscillation is noticeably reduced, further confirming that gravity inhibits escape from the lower well under the effect of gravity bias.

Moreover, regardless of gravity and the initial state, the vacillating behavior consistently occupies the same V-shaped central region, indicating that both equilibria are accessible under those forcing conditions. Comparing Figs. 5(a) and 5(d) with Figs. 5(b) and 5(e) shows that this V-shaped region expands under gravity, implying that the system can achieve switching between the two stable states over a wider range of forcing parameters.

C. Bifurcation and chaos

1. Largest Lyapunov exponent

To further quantify the chaotic characteristics underlying the observed dynamic behaviors, we employ the largest Lyapunov exponent (LLE) $\lambda_{\max}$ as a systematic indicator. The LLE provides a definitive measure of orbital divergence, clearly distinguishing between regular (periodic/quasi-periodic) and chaotic dynamics.

To compute the Lyapunov exponents, the non-autonomous forced Duffing equation is first transformed into an autonomous system through variable substitutions

$$\begin{cases} u_1 = u, \\ u_2 = \dot{u}, \\ u_3 = \omega\tau. \end{cases} \tag{44}$$

Applying this transformation, Eq. (12) is converted into the following autonomous form:

$$\begin{cases} \dot{u}_1 = u_2, \\ \dot{u}_2 = -\delta u_2 + u_1 - p u_1^3 - \left(p - 1 - G\right) + F\cos u_3, \\ \dot{u}_3 = \omega. \end{cases} \tag{45}$$

The Lyapunov exponents are then numerically calculated using the standard algorithm [39]. With an initial trajectory divergence of $\|\Delta \boldsymbol{r}\| = 10^{-7}$, the exponents corresponding to the state variables u_1, u_2 and u_3 are computed and denoted as λ_1, λ_2 and λ_3, respectively. The LLE is subsequently determined as $\lambda_{\max} = \max(\lambda_1, \lambda_2, \lambda_3)$. For the representative case of $Q = 5.22$, the spatial distributions of the LLE are presented in Figs. 6(a) and 6(b), for initial conditions starting from the upper stable state $(u,\dot{u}) = (u_{f1}, 0)$ and the lower stable state $(u,\dot{u}) = (u_{f3}, 0)$, respectively.

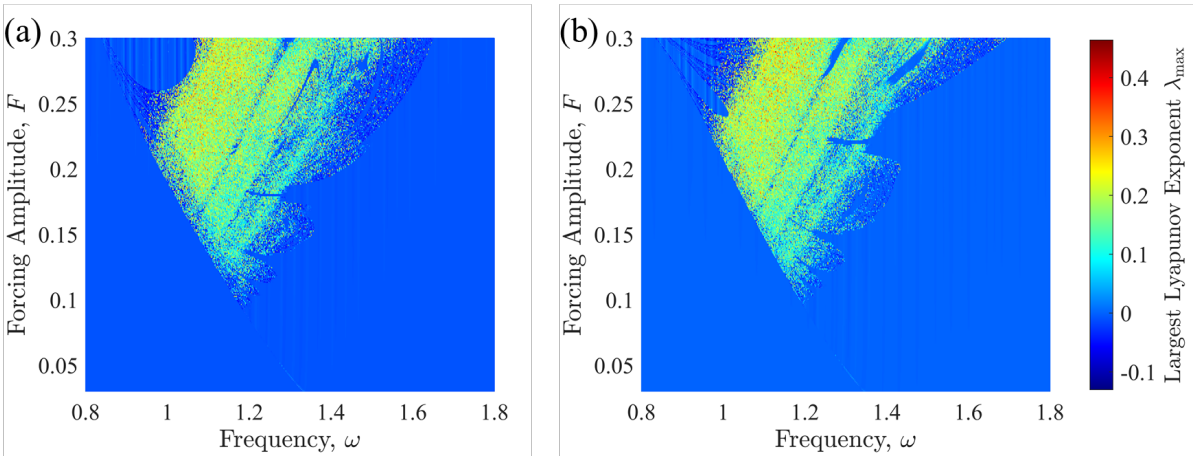

FIG. 6. Parameter maps of the largest Lyapunov exponent (LLE) $\lambda_{\max}$ in the (F,ω) space at $Q = 5.22$, evaluated for initial conditions starting from (a) the upper stable state $(u,\dot{u}) = (u_{f1}, 0)$ and (b) the lower stable state $(u,\dot{u}) = (u_{f3}, 0)$.

Figure 6 reveals several dynamical features characteristic of a double-well Duffing oscillator. In both panels (a) and (b), the left boundary of the V-shaped region separating regular and chaotic motion is sharp, particularly within the frequency range $1.0 < \omega < 1.2$. This clear demarcation reflects an abrupt transition from regular to chaotic motion with slight increases in either forcing amplitude or frequency—a behavior indicative of a subcritical saddle-node bifurcation [32,40]. At this boundary, the disappearance of the intra-well non-resonant attractor leads to a sudden transition to the other stable state or the emergence of a chaotic attractor, with the new attractor inheriting the basin of the former.

Notably, the upper-left part of the V-shaped region ($0.9 < \omega < 1.1$) exhibits more regular dynamics compared to the rest of the chaotic domain, which is accounted for by the dominance of cross-well period-1 oscillations in this parameter region [33,40]. Furthermore, several periodic windows are embedded within the broader chaotic sea, reflecting the rich and varied nonlinear phenomena present in the system.

2. Bifurcation computation and theoretical prediction

The parameter maps of the LLE in the (F,ω) space provide a comprehensive overview of chaotic behaviors in the curved beam dynamics. To gain deeper insight into the

transition mechanisms between different dynamical regimes, we further examine the system's behavior through bifurcation analysis.

Guided by the LLE maps, we construct bifurcation diagrams by fixing either the forcing frequency ω or amplitude F while varying the other parameter. Specifically, diagrams are generated for fixed frequencies $\omega = 1.05$ and $\omega = 1.30$, and fixed amplitudes $F = 0.20$ and $F = 0.28$, with simulations initiated from both stable states. To eliminate transient effects, data recording begins at $T_{\text{start}} = 400T$ and ends at $T_{\text{end}} = 800T$, where $T = 2\pi/\omega$. A uniform step size of $\Delta F = 0.001$ or $\Delta\omega = 0.001$ is used in the parameter variation.

The numerically computed bifurcation diagrams are presented in Figs. 7(c)–(j), along with the corresponding LLE charts in Figs. 7(a) and 7(b) for comparison. Black dashed lines in the LLE diagrams indicate the specific parameter values at which the bifurcation diagrams are computed.

As shown in Fig. 7(c), under $\omega = 1.05$, the oscillation originates as an intra-well motion within the upper potential well. With increasing forcing amplitude, the system undergoes an abrupt transition to the lower stable state. This jump results from the disappearance of the intra-well non-resonant attractor via a subcritical saddle-node bifurcation, corresponding to the left boundary of the V-shaped region in the Lyapunov exponent diagram Fig. 7(a). Owing to the combined effects of geometric asymmetry and gravity bias, the lower stable state at $Q = 5.22$ lies in a deeper potential well than the upper one, as illustrated in Fig. 2(f). This depth creates a range of forcing amplitudes over which the system vibrates around the lower equilibrium. This phenomenon is not observed in symmetric Duffing oscillators, where the bifurcation occurs simultaneously in both potential wells [40], highlighting the significant influence of the pre-curved shape and gravity. As the forcing amplitude continues to increase and eventually triggers the saddle-node bifurcation of the lower well, the system quickly transitions into chaotic motion through a subduction bifurcation. A period-3 window is also observable within the chaotic region. Finally, when the forcing amplitude becomes sufficiently large, the chaotic attractor vanishes due to a homoclinic bifurcation, leaving the cross-well period-1 attractor as the only stable solution of the system.

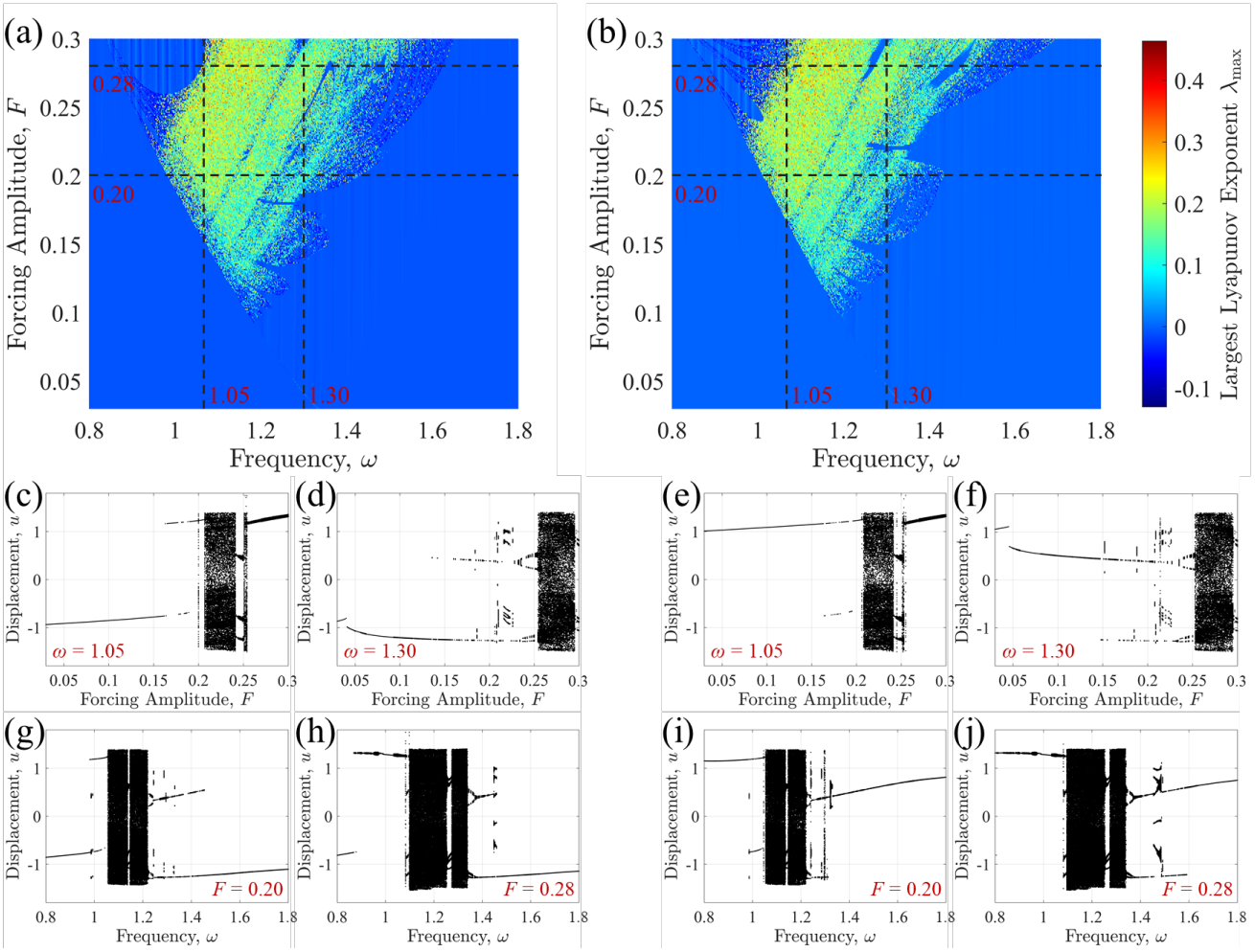

FIG. 7. Comparison of numerically computed bifurcation diagrams and LLE spectra at $Q = 5.22$, evaluated for initial conditions starting from the upper stable state $(u, \dot{u}) = (u_{\text{fl}}, 0)$ (panels (a), (c), (d), (g), (h)) and the lower stable state $(u, \dot{u}) = (u_{\text{f3}}, 0)$ (panels (b), (e), (f), (i), (j)). (a), (b) LLE diagrams with black dashed lines indicating parameter values corresponding to the bifurcation diagrams below. (c), (d) Bifurcation diagrams for the upper well under $\omega = 1.05$ and $\omega = 1.30$, respectively. (e), (f) Bifurcation diagrams for the lower well under $\omega = 1.05$ and $\omega = 1.30$, respectively. (g), (h) Bifurcation diagrams for the upper well under $F = 0.20$ and $F = 0.28$, respectively. (i), (j) Bifurcation diagrams for the lower well under $F = 0.20$ and $F = 0.28$, respectively.

Comparing with Fig. 7(c), a key difference in the dynamics observed in Fig. 7(e), where motion initiates from the lower stable state, lies in the fact that the subcritical saddle-node bifurcation has already occurred in the upper equilibrium by the time it takes place in the lower state. Consequently, the system undergoes an abrupt transition directly from intra-well motion to chaos, with almost no intermediate switching behavior.

Figures 7(d) and 7(f) reveal the bifurcation mechanism associated with the right boundary of the V-shaped region in the LLE diagram. As the forcing amplitude increases, the system first undergoes a subcritical saddle-node bifurcation, marked by a sudden jump in the response, leading to large-amplitude intra-well oscillations. The system subsequently exhibits intra-well motion, followed by switching and reverting dynamics, until it reaches the threshold of a period-doubling bifurcation. A cascade of period-doublings then drives the transition into chaotic motion. A period-5 window is also visible near the rightmost extremity of both diagrams.

For a fixed forcing amplitude of $F = 0.20$, as shown in Figs. 7(g) and 7(i), the system response evolves with increasing frequency. It begins with intra-well motion, followed by a regime of switching and reverting dynamics. As the frequency continues to rise, the system transitions into chaotic motion, within which a period-5 window is observed. Near the high-frequency end of the chaotic region, a period-doubling bifurcation occurs, eventually leading the system back to intra-well oscillation under sufficiently large forcing frequency.

In contrast, at the higher forcing amplitude of $F = 0.28$ (Figs. 7(h) and 7(j)), the evolutionary path differs. The system initially transitions to cross-well period-1 motion before evolving into chaos. Notably, the chaotic region in this case exhibits both period-3 and period-5 windows.

Furthermore, the theoretical models established in Section II, Part B are applied to predict the boundaries of the saddle-node and period-doubling bifurcations. The results are presented in Fig. 8, where the subcritical saddle-node and period-doubling bifurcations are indicated by the black dashed and white dash-dotted curves, respectively. Nevertheless, it should be noted that the theoretical scheme for the period-doubling bifurcation fails to accurately capture the right boundary of the central V-shaped vacillating region, due to the complex fractal patterns of switching and reverting behaviors in the nearby area. To address this problem, we adjust the computation of the amplitude a_1 for the basic period-1 solution in Eq. (33), which is now approximated numerically as $(u_s^{max} - u_s^{min})/2$, where u_s^{max} and u_s^{min} are the maximum and minimum values of the steady-state response $u(\tau)$ over the last ten oscillation cycles.

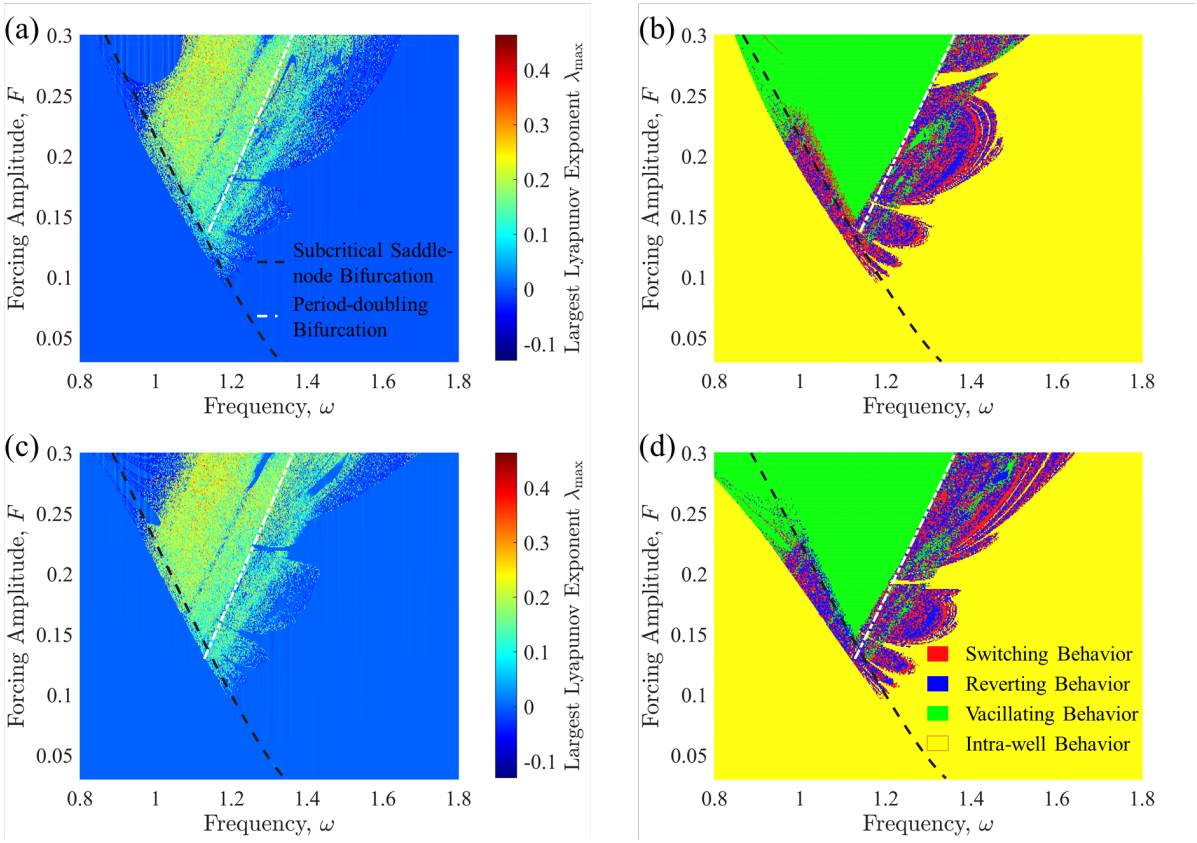

FIG. 8. Comparison of numerical and theoretical results in the (F,ω) parameter space at $Q = 5.22$. Subplots (a) and (c) contrast the theoretically predicted bifurcation boundaries (black dashed curve: subcritical saddle-node, white dash-dotted curve: period-doubling) with numerically computed LLE diagrams. Subplots (b) and (d) contrast the same theoretical boundaries with numerical steady-state behavior patterns. Results for two initial conditions are shown: (a), (b) start from the upper stable state $(u,\dot{u}) = (u_{f1},0)$, and (c), (d) start from the lower stable state $(u,\dot{u}) = (u_{f3},0)$.

As illustrated in Fig. 8, the theoretical curve for the subcritical saddle-node bifurcation aligns well with the left boundary of both the LLE diagram and the central V-shaped vacillating region. The right boundary of the vacillating region, on the other hand, is well predicted by the period-doubling bifurcation curve. This prediction is also supported by the bifurcation diagrams in Figs. 7(d) and 7(f), and Figs. 7(g)–(j). Moreover, as observed in the figures, when the motion initiates from the upper stable state, the subcritical saddle-node bifurcation requires a larger forcing amplitude and frequency to occur. This trend is consistent with the behavioral patterns shown in Figs. 7(c) and 7(e), as well as Figs. 7(g) and 7(i).

IV. EXPERIMENTS

A. Fabrication and experimental setup

To validate the theoretical and numerical results, experimental investigations were conducted. We fabricated the elastic bistable curved beams using PDMS (Sylgard 184, Dow Corning). The molds were printed with a fused-deposition 3D printer (Bambu H2D) using Bambu TPU 95A HF filament, with the bottom surface of the mold oriented perpendicular to the beam width. The PDMS base and curing agent were mixed at a weight ratio of 10:1. The mixture was then degassed by keeping it at −1 °C for 6 hours, poured into the mold, and finally cured at 60 °C for 4 hours.

Uncertainties in the elastic modulus, arising from small residual bubbles and nonuniform curing conditions [41,42], lead to noticeable sample-to-sample variations. To account for this, the elastic modulus was calibrated for each beam by matching the measured natural frequency in the upper stable state with its analytical prediction. Three beams with identical thickness (c = 6 mm) but varying arch heights (L = 18, 15, and 12 mm) were fabricated, all with a width of 20 mm and a span of 180 mm. These are labeled Beam 1, Beam 2, and Beam 3 in order of decreasing arch height.

Due to the practical difficulty in applying a distributed force excitation directly, a base excitation approach was adopted. The dynamic equation under base excitation was derived and compared with its force-excitation counterpart, thereby establishing a relationship between the forcing amplitude and the base acceleration amplitude (see Supplemental Material, Sec. S4 [31] for detailed derivation). This relationship enables the direct comparison of simulation and experimental results.

The elastic bistable curved beam was mounted on an electrodynamic shaker using a 3D-printed fixture. Figure 9(a) shows the two stable states—upper and lower—of the pre-shaped curved beam (Beam 1) in its mounted configuration. Manual switching between these states is demonstrated in Video S1 [31]. The shaker was aligned to oscillate parallel to the direction of gravity, ensuring the gravitational bias acted consistently on the beam. Two non-contact laser displacement sensors were employed: one to record the absolute displacement of the shaker table, and the other to measure the absolute displacement at the beam apex. Their difference yields the relative displacement due to the beam's elastic deformation. A built-in accelerometer on the shaker provided the feedback signal for precise closed-loop control of the excitation frequency $\hat{f}_{\text{base}}$ and the acceleration amplitude $\hat{a}_0$. In the following, all excitation amplitudes are normalized and reported in units of gravitational acceleration, $\hat{g}$ = 9.8 m/s^2.

To verify the numerically predicted steady-state behavior patterns, the excitation frequency and acceleration amplitude were systematically varied. However, given the high sensitivity of nonlinear systems to minor perturbations, a detailed point-by-point comparison of specific behavioral patterns between simulation and experiment is neither practical nor necessary. Therefore, following the definitions from the numerical analysis, motions involving transitions between the two stable states were identified as inter-well oscillations, whereas those confined to a single potential well were identified as intra-well oscillations. Validation of the numerical model was then based on the agreement between the predicted and experimentally observed regions of inter-well motion.

The procedure for identifying the boundary between these two regimes is illustrated in Video S2 [31]. For a fixed excitation frequency, the acceleration amplitude was increased stepwise. If no inter-well transition occurred within a prescribed observation period, the amplitude was further increased until a state transition was observed, thereby marking the boundary.

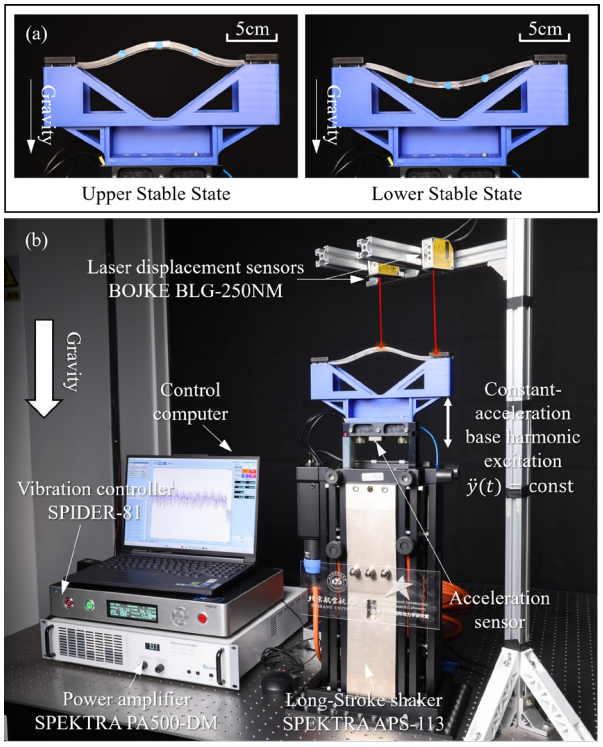

FIG. 9. Experimental setup. (a) Two stable states of the bistable curved beam. (b) Photograph of the setup for base excitation under constant harmonic acceleration.

B. Steady-state behaviors identification

To illustrate the four typical steady-state behaviors identified numerically in Sec. III.B, we present the corresponding experimental time-domain responses using Beam 1 as an example in Fig. 10 and Fig. 11. Specifically,

Figs. 10(a) and 10(b) show intra-well oscillations about the upper and lower stable states, respectively, while Fig. 10(c) displays vacillating dynamics. In these plots, the blue and red curves represent the base displacement and the beam's absolute displacement, respectively. The beam's displacement is referenced to the lower stable state (set to zero), with upward direction defined as positive.

Figure 10(a-i) shows an intra-well oscillation confined to the lower potential well. Because the features are not clearly discernible at the original scale, a zoomed view of the phase portrait is provided in Fig. 10(a-ii). This zoomed view reveals a triple-loop structure, indicating the emergence of a period-multiplied (period-3) response component. Vacillating dynamics are presented in Fig. 10(c-i), with its phase portrait [Fig. 10(c-ii)] clearly demonstrating repeated switching between the two stable states. Videos S3 and S4 [31] provide the experimental recordings for these cases, respectively.

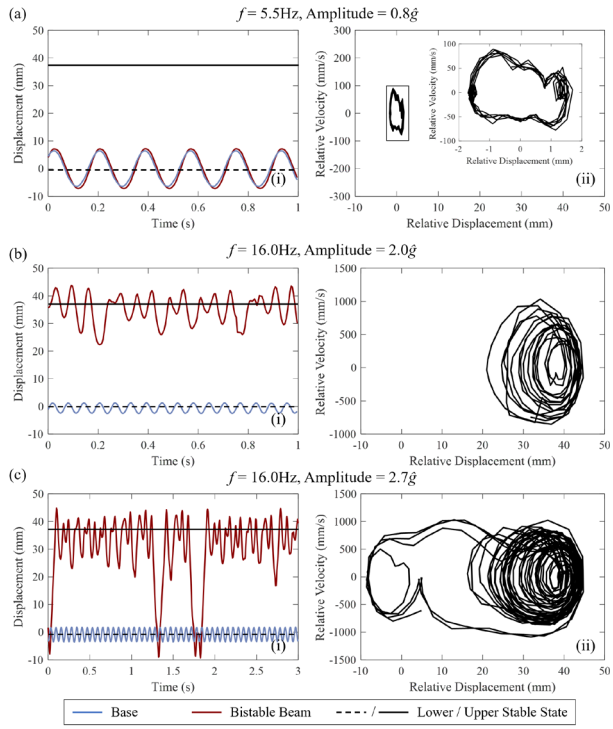

FIG. 10. Time-domain responses of Beam 1. (a), (b) Intra-well periodic oscillations about the lower and upper stable states, respectively. (c) Vacillating dynamics. Each panel includes an inset: (i) time-domain response of the absolute displacement; (ii) phase portrait (relative displacement vs. relative velocity).

By tuning the excitation frequency and acceleration amplitude, both switching and reverting behaviors can be realized. Figures 11(a) and 11(b) show switching from the lower to the upper state and the upper to the lower state, respectively. Correspondingly, Figs. 11(c) and 11(d) display reverting behaviors initiated from the upper and lower states. Experimental recordings of these dynamics are provided in Videos S5 and S6 [31].

C. Behavior boundaries comparison

To validate the theoretical model, we further compare the boundaries of inter-well and intra-well motions obtained from numerical computation and experiments under varying initial conditions and geometric parameter Q, as illustrated in Fig. 12. In the figure, the solid black curves denote the theoretical boundaries, the red dots represent the experimental data (see Supplemental Material, Sec. S5 [31] for original experimental data), and the blue curves show the interpolated experimental boundaries. As shown in the figure, the experimental results generally align with the theoretically predicted boundaries. However, as the geometric parameter Q increases, the deviation between experimental outcomes and theoretical boundaries becomes more pronounced. This growing discrepancy arises because a larger as-fabricated height h amplifies the system's nonlinearity, while the first-mode approximation becomes insufficient to fully capture the complete dynamic behavioral landscape of the curved beam [43].

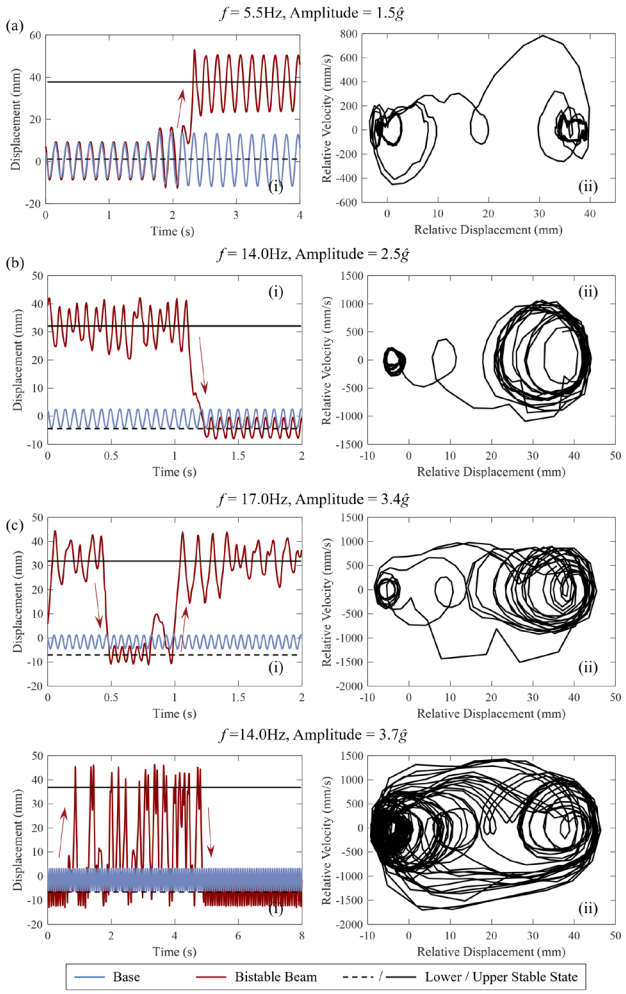

FIG. 11. Time-domain responses of Beam 1. (a), (b) Switching from the lower to the upper state and the upper to the lower state, respectively. (c), (d) Reverting behaviors starting from the upper and lower states, respectively. Each panel includes an inset: (i) time-domain response of the absolute displacement; (ii) phase portrait (relative displacement vs. relative velocity).

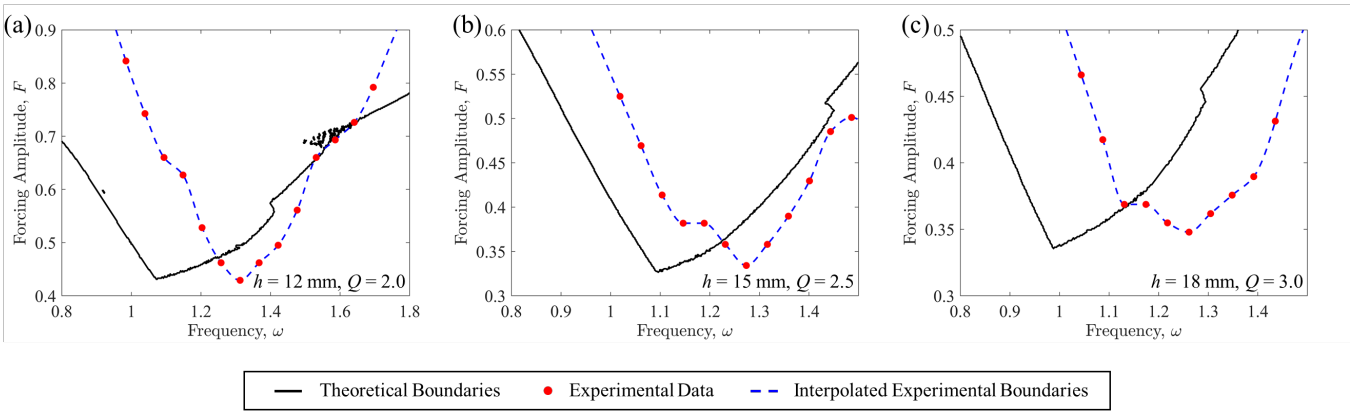

FIG. 12. Comparison of numerical and experimental results in the (F,ω) parameter space for different values of Q (adjusted via the as-fabricated height h). Simulations and experiments are all initialized from the upper stable state $(u,\dot{u})=(u_{\mathrm{fl}},0)$. In each panel, the solid black curve denotes the numerically predicted boundary between inter-well and intra-well behaviors; red dots represent experimental data; and the blue curve is an experimental boundary interpolated from these points. Specific parameters are: (a) h = 12 mm, Q = 2.0, (b) h = 15 mm, Q = 2.5, (c) h = 18 mm, Q = 3.0.

V. CONCLUSIONS

In summary, gravity has been incorporated into the theoretical model as a distributed bias. The complex nonlinear governing equation is reduced to a Duffing equation with a constant bias term. Since all parameters in the simplified equation are explicitly mapped to the material and geometric properties of the curved beam, it enables a systematic investigation into the system's behaviors, particularly its nonlinear dynamics. Analysis of the nonlinear restoring force and potential energy landscapes shows that the gravity bias shifts the force-displacement curve downward and deepens the potential well of the lower stable state.

Dynamic analysis further identifies the steady-state behavior patterns of the curved beam. Consistent with previous findings that the addition of a constant bias force reshapes dynamic patterns, our numerical simulations reveal that gravity bias facilitates inter-well motions, including switching, for an upward-curved beam when the motion initiates from the upper equilibrium, but suppresses such motions when starting from the lower equilibrium. The central vacillating region, however, expands under gravity force, enabling bidirectional switching regardless of the initial equilibrium. Moreover, for a fixed beam thickness c, both the switching and inter-well motion regions expand under a shallower arch height h when starting from the upper stable state, and contract when starting from the lower one. The LLE spectra and bifurcation diagrams further elucidate the bifurcation and chaotic characteristics of the system and validate the theoretically computed boundaries of the V-shaped vacillating regions.

To validate the reduced model, experimental studies were conducted. Due to the difficulty of applying distributed force excitation, base excitation was adopted, with rigorous transformation relationships established between two loading cases. The experiments clearly reproduced the four predicted steady-state behaviors. Comparison between numerical and experimental results confirms that the simplified Duffing-type model, despite its simplicity, successfully captures the essential nonlinear dynamics of the gravity-biased curved beam, including the distinct inter-well and intra-well motion patterns.

While the observed discrepancies under large geometric parameter Q indicate stronger nonlinearity beyond the scope of the present formulation, the model provides critical insights into how gravity bias systematically regulates the dynamic switching behavior and stability landscapes. This understanding is directly exploitable for designing and controlling bistable curved structures in applications where predictable state-switching under bias is required, such as in MEMS devices for low-power sensing or actuation, and in deployable or reconfigurable structures for aerospace and marine systems, where energy efficiency is paramount.

ACKNOWLEDGMENTS

This project has received funding from National Natural Science Foundation of China (Grant No. 92271104, 12102017) and Beijing Natural Science Foundation (Grant No. 1232014).

[1] Y. Cao, M. Derakhshani, Y. Fang, G. Huang, and C. Cao, Adv. Funct. Mater. **31**, 2106231 (2021).
[2] Y. Chi, Y. Li, Y. Zhao, Y. Hong, Y. Tang, and J. Yin, Adv. Mater. **34**, 2110384 (2022).
[3] Z. Zhang, L. W. Chen, and Z. D. Xu, Smart Mater. Struct. **31**, 105004 (2022).
[4] C. Zhang, X. Yin, R. Chen, K. Ju, Y. Hao, T. Wu, J. Sun, H. Yang, and Yan Xu, Smart Mater. Struct. **33**, 093001 (2024).
[5] R. Xu, C. Chen, J. Sun, Y. He, X. Li, M. H. Lu, and Y. Chen, Int. J. Extrem. Manuf. **5**, 042013 (2023).
[6] M. Hwang, and A. F. Arrieta, Phys. Rev. E **98**, 042205 (2018).
[7] A. Pal, V. Restrepo, D. Goswami, and R. V. Martinez, Adv. Mater. **33**, 2006939 (2021).
[8] H. Hussein, F. Khan, and M.I. Younis, Sensor Actuat. A-phys. **306**, 111961 (2020).
[9] H. Hussein, F. Khan, and M. I. Younis, Smart Mater. Struct. **29**, 075033 (2020).
[10] S.-W. Huang, F.-C. Lin, and Y.-J. Yang, Sensor Actuat. A-phys. **310**, 111934 (2020).
[11] X. Liu, F. Lamarque, E. Doré, and P. Pouille, Smart Mater. Struct. **24**, 075028 (2015).
[12] Y. Fu and W. Liu, Compos. Struct. **258**, 113195 (2021).
[13] A. Rafsanjani, A. Akbarzadeh, and D. Pasini, Adv. Mater. **27**, 5931 (2015).
[14] Y. Zhang, M. Tichem, and F. van Keulen, Int. J. Mech. Sci. **193**, 106172 (2021).
[15] Y. Zhang, M. Velay-Lizancos, D. Restrepo, N. D. Mankame, and P. D. Zavattieri, Matter **4**, 1990 (2021).
[16] A. Pal and M. Sitti, Proc. Natl. Acad. Sci. U.S.A. **120**, e2212489120 (2023).
[17] X. Hou, T. Sheng, F. Xie, and Z. Deng, Compos. Struct. **335**, 118001 (2024).
[18] M. D. Williams, F. V. Keulen, and M. Sheplak, J. Appl. Mech. **79**, 011006 (2012).
[19] J. Qiu, J. H. Lang, and A. H. Slocum, J. Microelectromech. Syst. **13**, 137 (2004).
[20] M. Alturki and R. Burgueño, J. Appl. Mech. **86**, 091002 (2019).
[21] M. Alturki and R. Burgueño, Eng. Struct. **220**, 110753 (2020).
[22] J. Hua, H. Lei, C. F. Gao, X. Guo, and D. Fang, Extreme Mech. Lett. **35**, 100640 (2020).
[23] D. Restrepo, N. D. Mankame, and P. D. Zavattieri, Extreme Mech. Lett. **4**, 52 (2015).
[24] J. Mao, W. Gao, C. Liu, D. Cao, and S. Lai. Appl. Math. Mech. **46**, 2017 (2025).
[25] H. Ueno, H. Toshiyoshi, and T. Suzuki, Sensor Actuat. A-phys. **378**, 115750 (2024).
[26] M. N. Hasan, T. E. Greenwood, R. G. Parker, Y. L. Kong, and P. Wang, Phys. Rev. E **108**, L022201 (2023).
[27] M. N. Hasan, S. Paul, T. E. Greenwood, R. G. Parker, Y. L. Kong, and P. Wang, Extreme Mech. Lett. **76**, 102299 (2025).
[28] H. T. Zheng, H. Ding, Nonlinear Dyn. **113**, 27085 (2025).
[29] M. F. Ashby, *Materials Selection in Mechanical Design*, 4th ed. (Butterworth-Heinemann, Oxford, 2011).
[30] G. Librandi, E. Tubaldi, and K. Bertoldi, Phys. Rev. E **101**, 053004 (2020).
[31] See Supplemental Material [url] for a detailed derivation of the model, its bifurcation analysis, the experimental principles, and the raw experimental data, which includes Refs. [19,30,32,33,44,45].
[32] K. Yagasaki, J. Sound Vib. **190**, 587 (1996).
[33] W. Szemplińska-Stupnicka and J. Rudowski, Chaos **3**, 375 (1993).
[34] Y. Liu, K. Huang, and J. Zhang, Thin-Walled Struct. **219**, 114265 (2026).
[35] J. Zhang, C. Zhang, L. Hao, R. Nie, and J. Qiu, Appl. Phys. Lett. **111**, 064102 (2017).
[36] J. Zhang, Z. Wu, C. Zhang, L. Hao, R. Nie, and J. Qiu, Smart Mater. Struct. **28**, 055009 (2019).
[37] J. M. T. Thompson, P. R. Soc. Lond. A **421**, 195 (1989).
[38] L. N. Virgin. J. Sound Vib. 126, 157 (1988).
[39] G. Benettin, L. Galgani, A. Giorgilli, and J.-M. Strelcyn, Meccanica **15**, 9 (1980).
[40] *The Duffing Equation: Nonlinear Oscillators and their Behaviour*, edited by I. Kovacic, M. J. Brennan (John Wiley & Sons, West Sussex, 2011).
[41] I. D. Johnston, D. K. McCluskey, C. K. L. Tan, and M. C. Tracey, J. Micromech. Microeng. **24**, 035017 (2014).
[42] A. Mata, A. J. Fleischman, and S. Roy, Biomed. Microdevices **7**, 281 (2005).
[43] M. de Bono, T. L. Hill, R. M. J. Groh, and S. A. Neild, Proc. R. Soc. A **480**, 20240198 (2024).
[44] V. V. Bolotin, *The Dynamic Stability of Elastic Systems* (Holden-Day, San Francisco, 1964).
[45] C. Hayashi, *Nonlinear Oscillations in Physical Systems* (Princeton University Press, Princeton, NJ, 2014).